IEEE Open Journal of Antennas and Propagation

Received XX Month, XXXX; revised XX Month, XXXX; accepted XX Month, XXXX; Date of publication XX Month, XXXX; date of current version XX Month, XXXX.

Digital Object Identifier 10.1109/OJAP.2020.1234567

Polarization Controlled Dual-Polarized MIMO Antenna with Enhanced Isolation for Full-Duplex WBANs

AJEET THAKUR*, ASHWANI SHARMA*, *Senior Member, IEEE*, and IGNACIO J. GARCIA ZUAZOLA†, *Senior Member, IEEE*

[1]Electrical Engineering Department, Indian Institute of Technology Ropar, Punjab, India
[2]School of Computing and Digital Media, London Metropolitan University, London, UK

Corresponding author: Ignacio J. Garcia Zuazola (e-mail: i.garciazuazola@londonmet.ac.uk).

This work was supported in part by SERB, Department of Science & Technology, Government of India under Grant CRG/2022/007257.

ABSTRACT A polarization controlled dual-polarized multiple-input multiple-output (MIMO) antenna with enhanced isolation for full-duplex wireless body area network (WBAN) in the 5.8 GHz industrial, scientific, and medical (ISM) band is proposed. The advanced polarization control of each antenna element comprising the MIMO is realized by embedding tailored T-shaped strips within the transversal slots of a main diagonal cut in the ground plane, which effectively steer the surface currents to a favorable direction to achieve the desired polarization with enhanced isolation. By slotting the twin circular patch radiating elements and incorporating twin capacitively coupled stepped elements adjacent to their feeding terminals, the proposed low-profile design realizes good impedance matching, return loss, and bandwidth. Experimental results demonstrate isolation greater than 5 dB compared with existing designs, and we report inter-port isolation that exceeds 33 dB for the 150 MHz bandwidth, with a peak isolation of approximately 67 dB. As a result, the proposed antenna exhibits low envelope correlation coefficient (ECC), high diversity gain (DG), and acceptable total active reflection coefficient (TARC) and channel capacity loss (CCL). A prototype antenna was tested under structural deformation by bending it along a -45° direction, with a simulated specific absorption rate (SAR) of 0.258 W/kg on a human phantom, thereby validating the antenna's compliance with safety standards. The findings of this study demonstrate that the proposed design effectively addresses critical challenges in full-duplex WBAN antennas by enhancing port isolation, minimizing mutual coupling, and advancing polarization control, while maintaining a low-profile and low-complexity feeding network structure.

INDEX TERMS Polarization control, port isolation, dual-polarization, low profile, full-duplex MIMO.

I. INTRODUCTION

IN recent years, the growing demand for wearable electronics has been driven by the rapid miniaturization of wireless devices, the deployment of high-speed communication networks, and ongoing advancements in battery technology. Wearable devices are utilized extensively in various fields, including in defense, healthcare, and firefighting applications, where different antennas are employed to sense, collect, and exchange data between on-body sensors and off-body gateways [1], [2]. Unlike conventional antennas fabricated on rigid substrates, wearable antennas are preferable because of their low profile, flexibility, and physical robustness, while offering wide bandwidth performance and a reduced specific absorption rate (SAR) for improved electromagnetic (EM) safety.

For effective communication between on-body antennas and off-body terminals, full-duplex antenna systems [3], [4] enable simultaneous high-speed data transmission and reception within the same frequency band, effectively enhancing spectral efficiency compared with conventional half-duplex systems. In conventional systems, bidirectional communication is realized using a radio frequency (RF) switch, where the transmitter (Tx) and receiver (Rx) modules connect to a single-port antenna in an alternating manner using time-

This work is licensed under a Creative Commons Attribution 4.0 License. For more information, see https://creativecommons.org/licenses/by/4.0/

division duplexing (TDD). However, this time-sharing mechanism increases circuit complexity and limits both the overall efficiency and data throughput of the system. Alternatively, dual-port antenna configurations offer a simpler and more efficient solution [3]–[6], where one port is connected to the Tx module and the other to the Rx module. However, most available dual-port antenna designs [7], [8] are not suitable for full-duplex Tx/Rx operation because their ports typically operate at different frequencies and exhibit distinct radiation characteristics, resulting in inefficient spectrum utilization. Thus, dual-polarized full-duplex antennas are preferred for wireless body area network (WBAN) applications because polarization diversity facilitates seamless integration of the Tx and Rx antennas without compromising the size of the RF front-end system. Despite this advantage, achieving high isolation between the Tx and Rx is critical to suppress interference and reduce loading effects in the later stages of the transceiver.

Several methods have been investigated to mitigate mutual coupling between antenna ports, including EM bandgap (EBG) and high impedance surfaces (HIS) [9]–[11], metamaterials [12], [13], line patch [14], parasitic element resonators [15]–[18], and differential feeding networks [19], [20]. Furthermore, other methods, e.g., a circulator connected to a single antenna [21] or the use of metallic vias [22]–[25], demonstrate improved isolation. However, these methods often increase the antenna's footprint and design complexity. Thus, this study focuses on achieving high isolation in a lightweight and practical wearable design.

An alternative approach to enhance isolation and bandwidth simultaneously using integrated strips has been proposed previously [26]. Similarly, an HIS-integrated circular-shaped multiple-input multiple-output (MIMO) design [9] achieves port isolation exceeding 15 dB. Defected ground structures (DGS) [27]–[29], which modify the ground plane, have been investigated to improve key antenna parameters e.g., impedance, axial ratio bandwidth, cross-polarization, and port isolation, with reported 26, 18, and 20 dB isolation, respectively. In [30] and [31], isolation values greater than 12 dB and 22 dB were achieved using pattern and polarization diversity, respectively. However, despite these advancements, the existing methods [27]–[30] exhibit dipole-like radiation patterns, which worsens the SAR. Moreover, one previous design [31] has a high profile due to the use of a large reflector, which makes it unsuitable for compact WBAN applications. Thus, designing a low-profile, low-complexity, dual-polarized full-duplex wearable antenna with high isolation, a simple feeding structure, and a directional radiation pattern is a significant challenge.

To address this issue, this paper proposes a polarization controlled dual-polarized MIMO antenna with enhanced isolation for full-duplex WBAN applications in the 5.8 GHz industrial, scientific, and medical (ISM) band. Here, advanced polarization control of each antenna element comprising the MIMO is achieved by embedding tailored T-shaped strips within the transversal slots of a main diagonal cut in the ground plane. This effectively steers the surface currents in a favorable direction to achieve the desired polarization. In addition, by adding a slot in the twin circular radiating patches and incorporating twin capacitively coupled stepped elements adjacent to their feed terminals, the design achieves a low profile, low SAR configuration with enhanced bandwidth and improved isolation. The measured inter-port isolation exceeds 33 dB across the 5.8 GHz ISM band, with a peak isolation of approximately 67 dB under real-world measurements.

The remainder of this paper is organized as follows. The step-by-step antenna design is presented in Section II. The measured results, including on-body deployment performance, are validated in Sections III and IV. Section V presents an analysis of the MIMO performance. Finally, the paper is concluded in Section VI.

II. ANTENNA DESIGN

A. ANTENNA LAYOUT

As shown in Figure 1, the proposed design comprises two circular patch radiating elements printed on the upper surface of a semi-flexible material, i.e., RT/duroid 5880 ($\varepsilon_r = 2.2$, $\tan\delta = 0.0009$), with overall dimensions of $L_{sub} \times L_{sub} \times t$ (48 mm $\times$ 48 mm $\times 1.57$ mm). A slot is inserted in each of the circular radiating patches ($\#Tx$ and $\#Rx$), and each patch is excited via a $50\ \Omega$ microstrip line. Two capacitively coupled stepped elements are incorporated adjacent to the feeding terminals to enhance both the bandwidth and the isolation between Port 1 (designated P_1:Tx) and Port 2 (designated P_2:Rx), as shown in Figure 1(a). The advanced polarization control of each antenna element comprising the MIMO is implemented by embedding tailored T-shaped strips within transversal slots of a main diagonal cut in the ground plane, as shown in Figure 1(b). The antenna design is performed using the commercially available EM solver ANSYS HFSS. Initially, the radius r of the twin circular radiating patches is calculated as follows [29]:

$$f_r = \frac{1.8412 \cdot c}{2\pi R_{\text{eff}}\sqrt{\varepsilon_r}} \tag{1}$$

$$R_{\text{eff}} = r\sqrt{1 + \frac{2t}{\pi r \varepsilon_r}\left[\ln\left(\frac{\pi r}{2t}\right) + 1.7726\right]} \tag{2}$$

where f_r, c, R_{eff}, ε_r, and t denote the resonant frequency, the speed of light in vacuum, the effective radius of the patch, the relative permittivity of the substrate, and the substrate thickness, respectively.

B. DESIGN APPROACH

Following the calculation of the slotted circular radiating patches (Section II-A), the step-by-step design evolution of the proposed MIMO antenna is presented. The evolution process is divided into four stages (Stage-1 to Stage–4), as shown in Figure 2(a).

This article has been accepted for publication in IEEE Open Journal of Antennas and Propagation. This is the author's version which has not been fully edited and content may change prior to final publication. Citation information: DOI 10.1109/OJAP.2025.3648623

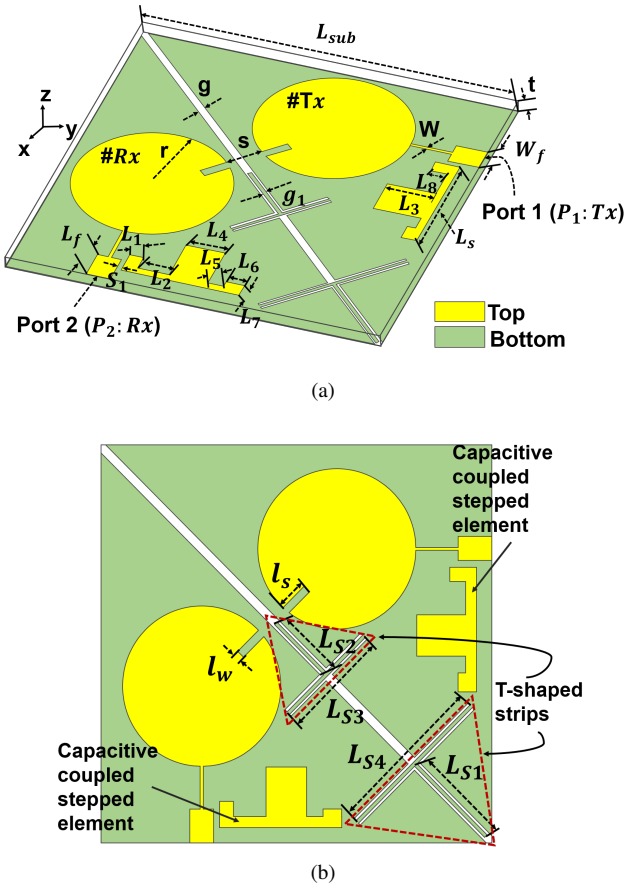

FIGURE 1. **Layout of the proposed wearable full-duplex MIMO design with optimized parameters (a) Perspective view. (b) Top view. Here,** $g = 1$, $s = 4.45$, $t = 1.57$, $r = 9.8$, $W = 0.4$, $g_1 = 0.5$, $L_1 = 1.77$, $L_2 = 4$, $L_3 = 6.1$, $L_4 = 5$, $L_5 = 2$, $L_6 = 2.327$, $L_7 = 2$, $L_8 = 3.11$, $L_f = 4$, $L_s = 15.1$, $L_{sub} = 48$, $W_f = 3$, $L_{S1} = 12.4$, $L_{S2} = 8.75$, $L_{S3} = 13$, $L_{S4} = 13.788$, $l_s = 3.589$, $l_w = 1.1$, $S_1 = 0.23$ **(units: mm).**

In Stage-1, two slotted circular radiating patches are introduced, which are positioned close to each other and orthogonally oriented. They are fed by 50 Ω microstrip lines connected to ports P_1: Tx and P_2: Rx, resonating at 5.776 GHz with good impedance matching ($|S_{11}|; |S_{22}| < -10$ dB), as shown in Figure 2(b). The slots on the patches are strategically etched to improve impedance matching and shift the resonant frequency (f_r) closer to the desired operating frequency (f_0) by adjusting the effective length and current paths on the patches.

In Stage-2, two capacitively coupled stepped elements are introduced near the microstrip lines without affecting the total dimensions of the proposed antenna. Note that the initial L_s value is selected as half the guided wavelength ($\lambda_g/2$) at 5.8 GHz, resulting in $L_s = 17.92$ mm. As shown in Figure 2(b), these elements enhance the impedance bandwidth without increasing the substrate thickness or antenna size. The Stage-1 design resonates at 5.776 GHz; however, Stage-2 exhibits two distinct resonances at 5.765 GHz and 5.90 GHz. The second resonant frequency (f_{SL}), which is generated by the capacitively coupled stepped elements, combines

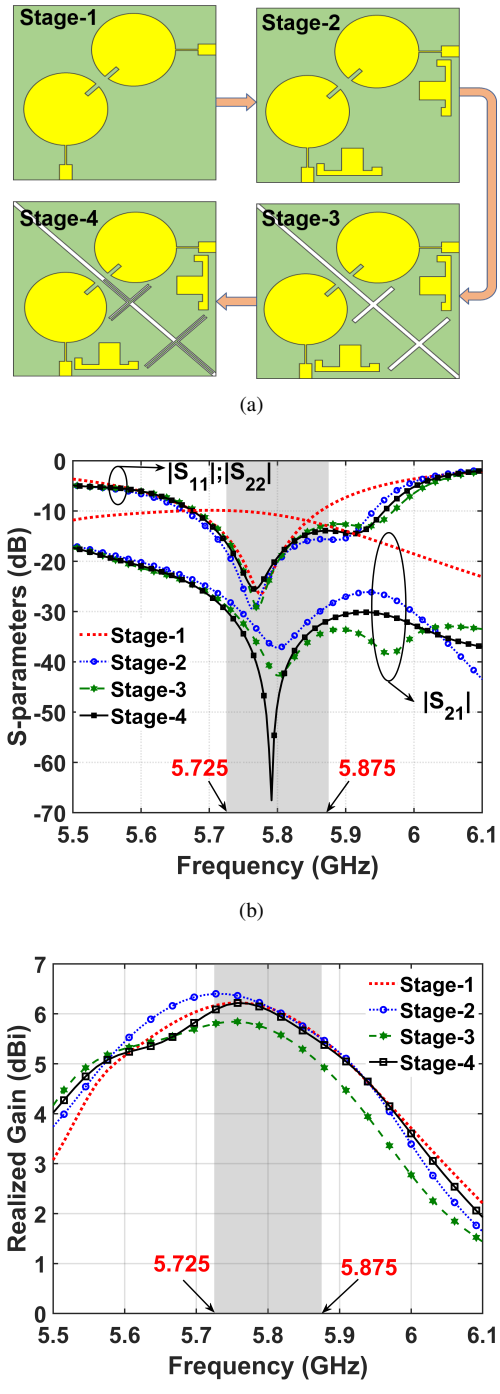

FIGURE 2. **Evolution of the proposed antenna from Stage-1 to Stage-4 (a) Development Stages. (b) Simulated S-parameters. (c) Realized gain (dBi).**

with the first resonant frequency (f_{CP}) of the slotted circular patch to form a broader impedance bandwidth. The influence of the stepped elements on $|S_{11}|; |S_{22}|$ is further investigated in Section II-E. Compared with Stage-1, Stage-2 enhances the impedance bandwidth from 180 MHz ($FBW = 3\%$) to approximately 280 MHz ($FBW = 4.8\%$), with slightly improved $|S_{11}|; |S_{22}|$ and noticeably better isolation $|S_{21}|$.

In Stage-3, a main diagonal cut is introduced in the ground plane to reduce the mutual coupling between the $\#Tx$ and $\#Rx$ elements, effectively enhancing the isolation between ports P_1:Tx and P_2:Rx (Figure 2(b)). The isolation is further improved by incorporating two additional transversal slots. In Stage-4, the advanced polarization control of each antenna element comprising the MIMO is achieved by embedding tailored T-shaped strips within the transversal slots, effectively steering the surface currents in a favorable direction to realize the desired polarization. This mechanism is analyzed in Section II-C. As shown in Figure 2(c), preliminary results indicate that the realized gain decreases from Stage-2 to Stage-3, primarily due to an energy drop through the slots in the ground plane. However, this gain reduction is compensated in Stage-4 by introducing the T-shaped strips, which improves the front-to-back radiation performance.

C. POLARIZATION CONTROL WITH ENHANCED ISOLATION

The electric (E-) and magnetic (H-) field distributions of the proposed design, from Stage-1 to Stage-4 with P_1:Tx excitation, are shown in Figure 3. The analysis is carried out at the center frequency of 5.8 GHz in the ISM band.

In Stage-1, the close proximity of the $\#Tx$ and $\#Rx$ radiating elements ($s = 0.09\lambda_0$, where λ_0 denotes the wavelength at the center frequency of the ISM band) results in strong E- and H-field coupling, as shown in Figure 3(a) for the E-field and Figure 3(b) for the H-field. This strong coupling results in poor port isolation ($|S_{21}| \approx -10$ dB), as shown in Figure 2(b). Then, in Stage-2, introducing the capacitively coupled stepped elements effectively reduces the mutual coupling. The added stepped elements cause the E- and H-field distributions to spread along the element adjacent to the excited port P_1:Tx, thereby reducing the coupled fields towards the other slotted circular patch ($\#Rx$), as shown in Figures 3(c) and 3(d). Compared with the Stage-1 design, Stage-2 achieves approximately 16 dB enhanced isolation in the targeted ISM band ($5.725 - 5.875$ GHz).

In Stage-3, additional isolation enhancement is realized by incorporating slots into the ground plane, as is evident from the S-parameters shown in Figure 2(b). Here, the transversal slots, together with the main diagonal cut, disrupt the continuity of the ground plane currents and suppress surface wave excitation, thereby minimizing the coupling effect between the $\#Tx$ and $\#Rx$ elements, as shown in Figures 3(e) and 3(f). These slots help confine the field distributions in their proximity, creating a region of weak H-field around the $\#Rx$ element, as shown in Figure 3(f), which leads to improved isolation. This is validated by the S-parameter results presented in Figure 2(b). The distributions plotted in Figures 3(g) and 3(h) illustrate the E- and H-fields for the Stage-4 design, respectively. As can be seen, the coupled intensity at P_2:Rx is optimally minimized by inserting the T-shaped strips into the transversal slots of the main diagonal cut in the ground plane. This effectively

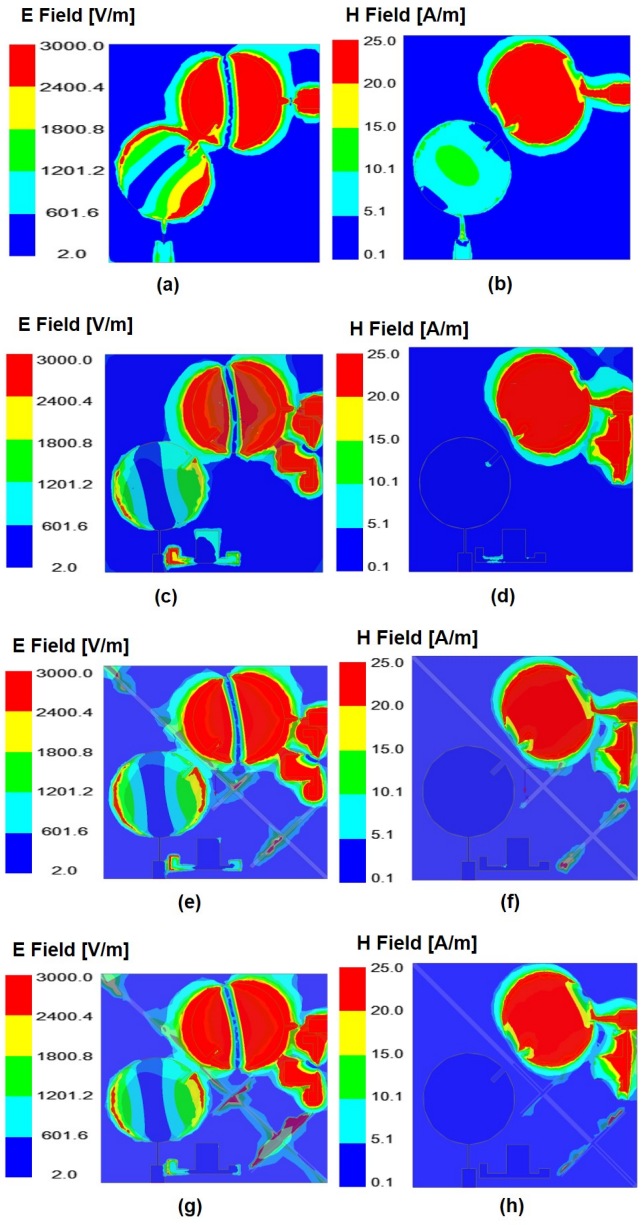

FIGURE 3. Field distributions of Stage-1 to Stage-4 at 5.8 GHz with P_1:Tx excitation: (a), (c), (e), (g) E-field. (b), (d), (f), (h) H-field.

enhances the isolation between the ports, as confirmed by the S-parameter simulations shown in Figure 2(b).

The isolation improvement is further analyzed by studying the surface current distributions on the radiating elements. The plots in Figures 4(a) and 4(b) show the surface current distributions at the coupling dip (CD) frequency (5.79 GHz; the closest to the center of the ISM band) for Stage-3 and Stage-4, respectively. In Stage-3 (Figure 4(a)), the currents on the $\#Rx$ element and the adjacent stepped element are largely perpendicular to each other. However, in Stage-4, embedding the tailored T-shaped strips within the transversal slots of the main diagonal cut in the ground plane causes the currents to oppose each other (Figure 4(b)).

This article has been accepted for publication in IEEE Open Journal of Antennas and Propagation. This is the author's version which has not been fully edited and content may change prior to final publication. Citation information: DOI 10.1109/OJAP.2025.3648623

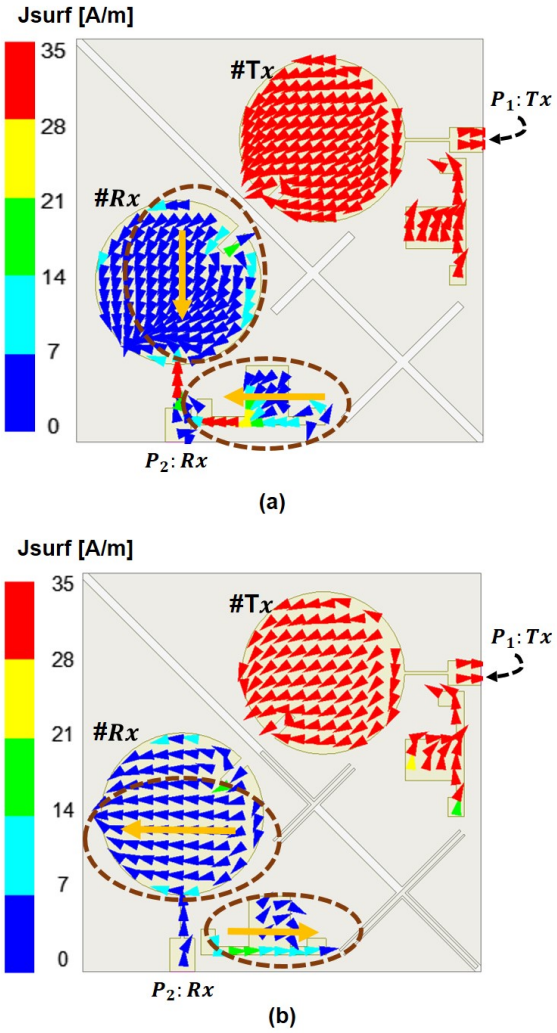

FIGURE 4. Vector surface current distribution for (a) Stage-3. (b) Stage-4.

This introduces a new method to customize the polarization of the $\#Rx$, which results in advanced polarization control of each antenna element comprising the MIMO, effectively steering the surface currents in a favorable direction for the desired polarization and enhancing isolation considerably. The improved isolation results in very little RF energy leakage from P_2:Rx, thereby reducing the mutual coupling between P_1:Tx and P_2:Rx. Thus, compared with the Stage-1 design, the Stage-4 design achieves an isolation improvement of greater than 20 dB within the targeted ISM band and over 15 dB across the overall antenna frequency band, with a peak isolation of 67.7 dB at 5.79 GHz (Figure 2(b)). Thus, the proposed technique achieves advanced polarization control with enhanced isolation; reciprocity is observed when P_2:Rx is excited and P_1:Tx is terminated with a matched load.

By analyzing the surface current distribution in Figure 4(b), it is evident that a distinct current component is observed on the capacitively coupled stepped element adjacent to the excited slotted circular patch. This current is oriented perpendicular to that on the excited slotted circular patch. Figure 5 shows the simulated Cartesian-plotted radiation patterns of the proposed design with and without the capacitively coupled stepped element, demonstrating a slight reduction in gain with a wider beamwidth without compromising other performance parameters. This validates the polarization control with enhanced isolation.

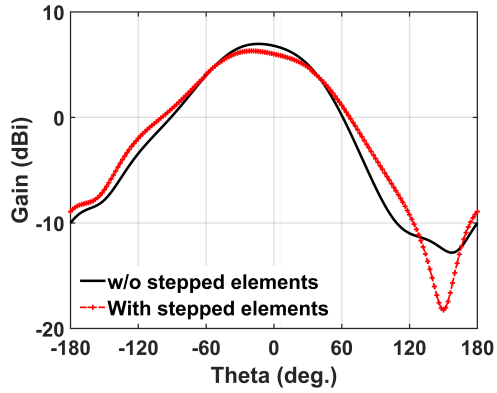

FIGURE 5. Simulated radiation pattern with and without (w/o) capacitively coupled stepped elements.

D. POLARIZATION CONTROLLED DUAL-POLARIZED MIMO ANTENNA-EQUIVALENT CIRCUIT MODEL

The predicted equivalent circuit model of the proposed design is shown in Figure 6. Each slotted circular radiating

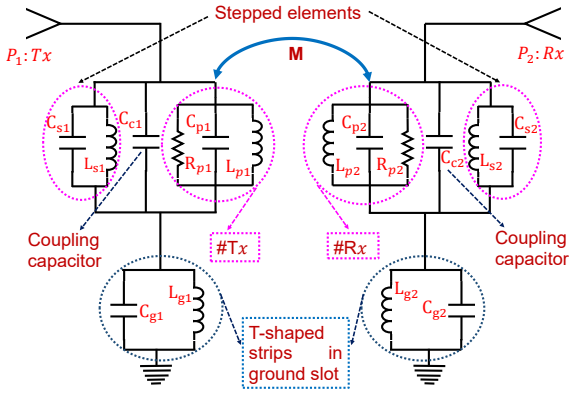

FIGURE 6. Equivalent circuit model of the proposed antenna.

element in the proposed design can be modeled as a parallel RLC resonator [32] ($R_{p1} = R_{p2} = R_p, L_{p1} = L_{p2} = L_p$, and $C_{p1} = C_{p2} = C_p$). The resonant frequency can be determined using

$$f_{CP} = \frac{1}{2\pi\sqrt{L_p C_p}}. \tag{3}$$

The identical capacitively coupled stepped elements, represented by a parallel LC circuit with $L_{s1} = L_{s2} = L_s$, and $C_{s1} = C_{s2} = C_s$, determine the secondary resonant frequency f_{SL}, which is greater than the f_{CP} due to the

smaller inductive and capacitive loading. The f_{SL} can be calculated as

$$f_{SL} = \frac{1}{2\pi\sqrt{L_s C_s}}. \tag{4}$$

A coupling capacitor $C_{c1} = C_{c2} = C_c$ represents the gap between the stepped element and the feedline and fine-tunes the interaction between the primary and secondary resonances. Note that both resonating modes occur within close proximity; thus, their interaction causes resonance merging, resulting in increased bandwidth. The resulting resonant frequency (merged) can be approximated as

$$f_{merged} = \frac{1}{2\pi\sqrt{L_{eff}(C_p + C_s)}} \tag{5}$$

where L_{eff} is the effective inductance accounting for the interaction of the two resonators, and $C_p + C_s$ represents the combined capacitance due to resonance merging.

Mutual coupling between the radiating elements occurs due to the near-field EM interactions, where energy from the excited element couples into the neighboring element, which degrades the isolation. The capacitively coupled stepped element, placed adjacent to the excited element, mitigates this effect by absorbing part of the energy before it reaches the neighboring element, thereby improving isolation. The mutual coupling coefficient is expressed as

$$k = \frac{M}{\sqrt{L_{p1} L_{p2}}}. \tag{6}$$

For identical antenna elements where $L_{p1} = L_{p2} = L_p$, this simplifies to

$$k_{original} = \frac{M_{original}}{L_p}. \tag{7}$$

By introducing the capacitively coupled stepped elements ($L_{s1} = L_{s2}$, and $C_{s1} = C_{s2}$), the mutual inductance is reduced to

$$M_{new} = M_{original} - \Delta M \tag{8}$$

where ΔM represents the mutual coupling reduction due to the stepped elements. Then, the updated mutual coupling coefficient is given by

$$k_{new} = \frac{M_{new}}{L_p} = \frac{M_{original} - \Delta M}{L_p}. \tag{9}$$

Here, $\Delta M > 0$; thus, it follows that

$$k_{new} < k_{original} \tag{10}$$

which confirms that the mutual coupling is reduced significantly, thereby leading to isolation improvement.

Next, the T-shaped strips embedded in the ground plane introduce additional inductive ($L_{g1} = L_{g2} = L_g$) and capacitive ($C_{g1} = C_{g2} = C_g$) effects, which in turn modify the surface current distribution and further suppress the inter-port coupling. These strips also provide support for the polarization control by steering the surface currents in a favorable direction. After incorporating these strips, the mutual inductance is

$$M_{final} = M_{new} - \frac{L_g C_g}{L_p}. \tag{11}$$

Thus, the final mutual coupling coefficient is expressed as

$$k_{final} = \frac{M_{final}}{L_p} = \frac{M_{original} - \Delta M - \frac{L_g C_g}{L_p}}{L_p}. \tag{12}$$

Here, $\Delta M > 0$ and $\frac{L_g C_g}{L_p} > 0$; thus, the final mutual coupling coefficient satisfies,

$$k_{final} < k_{new} < k_{original} \tag{13}$$

which ensures minimal inter-port interference and optimal full-duplex operation.

E. PARAMETRIC ANALYSIS

In the following, the proposed design is analyzed parametrically. Here, for conciseness, only the effects of the key parameters are presented, including the length of the capacitively coupled stepped element L_s (Figure 7(a)), the embedded T-shaped strips within the transversal slots of the main diagonal cut in the ground plane L_{S1} and L_{S2} (Figure 7(b)), the parameters L_{S1} and S_1 (Figures 8(a) and 8(b)), and the width g of the main diagonal cut (Figure 8(c)). Initially, the enhancement of the impedance bandwidth is analyzed by combining f_{CP} and f_{SL}. As shown in Figure 7(a), increasing L_s results in a downward shift of f_{SL}, while f_{CP} remains nearly unchanged. Consequently, the two resonant modes come close to each other, resulting in a broadened impedance bandwidth.

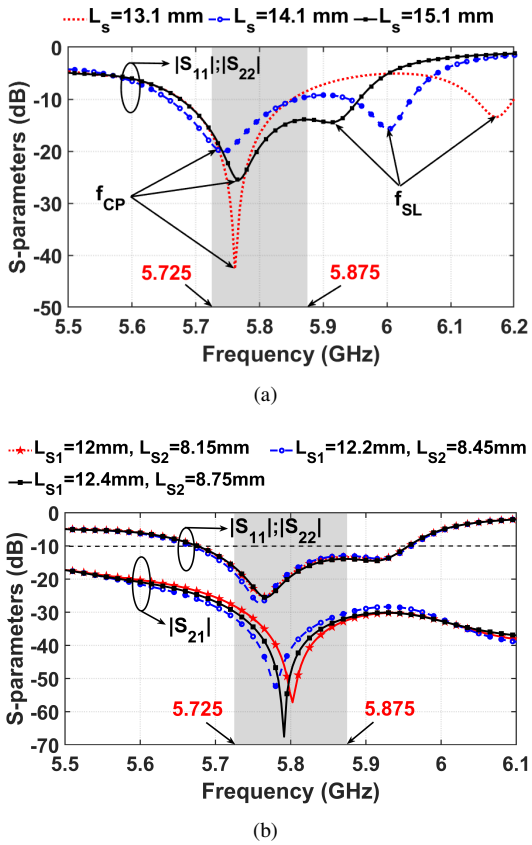

FIGURE 7. Simulated S-parameters for different lengths of (a) L_s. (b) L_{S1} and L_{S2}.

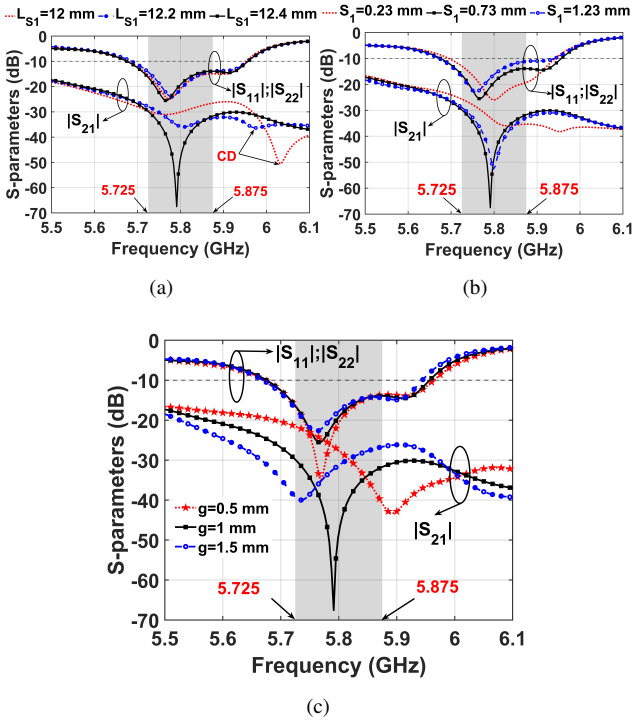

FIGURE 8. **Simulated S-parameters for different lengths of (a) L_{s1}. (b) S_1. (c) g.**

Figure 7(b) indicates that variations in L_{S1} and L_{S2} have minimal effect on impedance bandwidth and matching; however, this significantly enhances the mutual coupling performance within the desired frequency band. With an increase in L_{S1} and L_{S2}, the reflection coefficient $|S_{11}|;|S_{22}|$ remains nearly unaffected, and the decoupling dip improves and reaches a peak isolation of -67.7 dB at 5.79 GHz (the closest to the center of the ISM band).

The results presented in Figures 8(a) and 8(b) demonstrate the effects of varying the length of the T-shaped strip L_{S1} (while keeping L_{S2} unchanged) and the gap S_1 between the feed line and the stepped element on the S-parameters. Here, L_{S1} controls the optimal placement and tuning of the CDs [33], creating a notch at 5.79 GHz (the closest to the center of the ISM band). This establishes a stopband at this frequency, which effectively suppresses the unwanted signals within the targeted ISM band. However, the gap S_1, aids in impedance matching while tuning the CD, with optimal isolation and matching obtained when $S_1 = 0.73$ mm. Figure 8(c) shows the simulated S-parameters for different values of g. As can be seen, $|S_{11}|;|S_{22}|$ remains predominantly unaffected as g increases from 0.5 mm to 1.5 mm. However, the decoupling frequency decreases significantly from 5.89 GHz to approximately 5.71 GHz, and $|S_{21}|$ varies considerably. The optimal g value is determined to be 1 mm, which deviates from the conventional understanding that a wider slot in the ground plane between the antenna elements results in weaker mutual coupling. This improvement is attributed to the presence of the T-shaped strips embedded within the transversal slots of the main diagonal cut in the ground plane, which provide effective polarization control with enhanced isolation.

III. FABRICATION AND MEASURED RESULTS

The fabricated polarization controlled dual-polarized MIMO antenna is shown in Figure 9(a) and measured in a realistic environment. The experimental results validated the simulations, confirming the reliability of the proposed design/prototype.

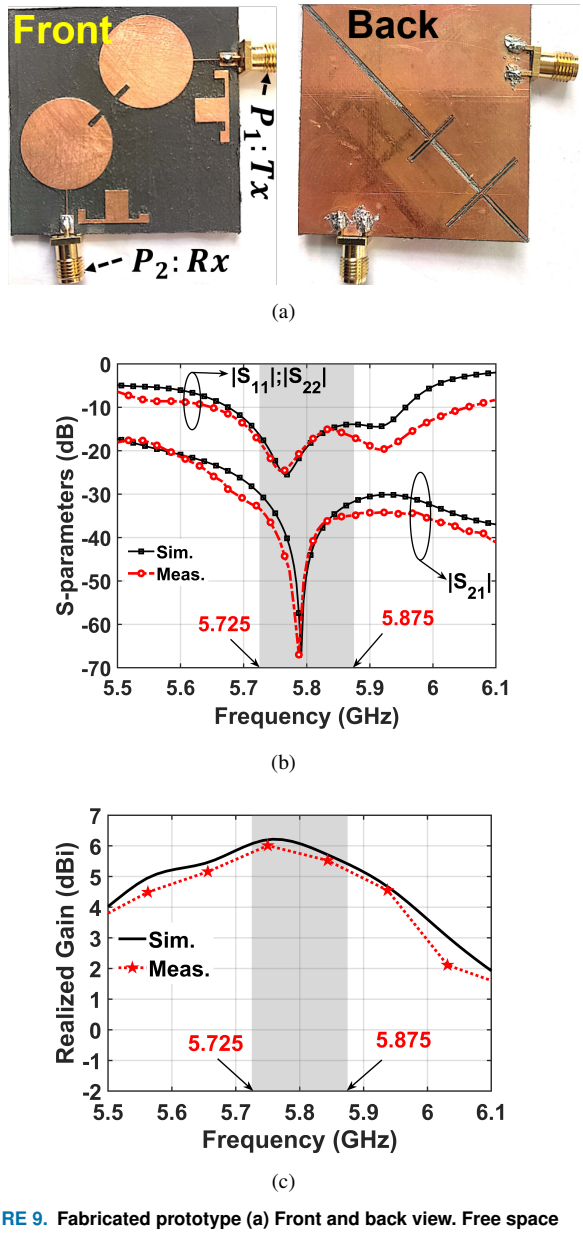

FIGURE 9. **Fabricated prototype (a) Front and back view. Free space simulations vs. measurements of (b) S-parameters and. (c) Realized gain (dBi).**

A. S-PARAMETERS RESULTS

The measured and simulated $|S_{11}|; |S_{22}|$ and $|S_{21}|$ results of the proposed design are shown in Figure 9(b), which compares the impedance bandwidth and port coupling in free space under flat (non-bent) conditions. Here, the measured impedance bandwidth with $|S_{11}|; |S_{22}|$ below -10 dB and $|S_{21}|$ of -26 dB is $5.645 - 6.05$ GHz ($FBW = 7.8\%$). Within the targeted ISM band, $|S_{21}|$ remains below -33 dB, thereby corroborating the simulations. In addition, two resonances are observed across the passband, corresponding to f_{CP} and f_{SL}. Thus, the proposed design successfully covers the desired ISM band ($5.725 - 5.875$ GHz).

B. ANTENNA GAIN

The simulated and measured gain of the proposed design in free space is shown in Figure 9(c). The results demonstrate good agreement between the measured and simulated gains throughout the operating band. Note that the slight discrepancies are attributed to potential tolerances in the fabrication process and measurements. Within the ISM band, the simulated peak realized gain is 6.2 dBi compared with 6.01 dBi in measurements. This corroborates the simulation and experimental results.

C. RADIATION PATTERNS

The simulated and measured normalized radiation patterns of the proposed design are shown in Figure 10. Both the E- and H-plane patterns exhibit hemispherical coverage when P_1:Tx and P_2:Rx are excited individually, with only minor differences between the measured and simulated results, which are likely caused by fabrication and measurement tolerances. The measured co- and cross-polarization isolation in both planes exceeds 18 dB, which indicates good polarization purity. However, this is less critical in mobile wearable applications because the primary objective of a dual-polarized antenna is to address polarization mismatch losses in off-body communications [26], [34]. The results are also evaluated under a bending radius of $R = 40$ mm in simulations. Although noticeable variations are observed compared with the flat condition ($R = \infty$), the antenna maintains performance that is suitable for wearable applications.

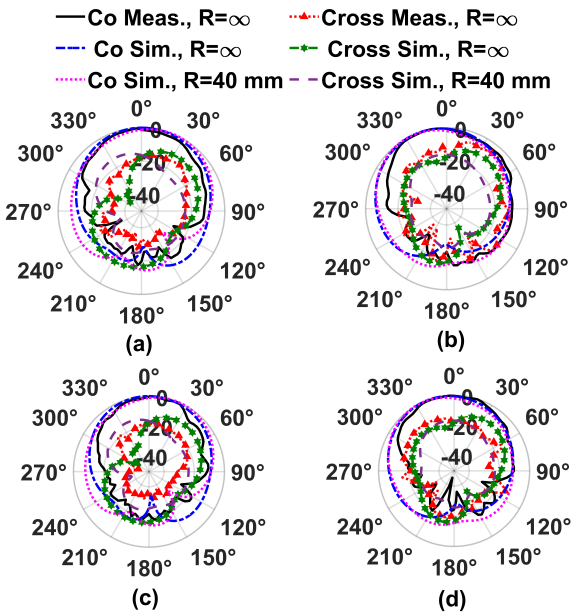

FIGURE 10. Normalized 2-D radiation patterns (dBi) of the proposed antenna at 5.8 GHz (a) E-plane, P_1:Tx is excited. (b) H-plane, P_1:Tx is excited. (c) E-plane, P_2:Rx is excited. (d) H-plane, P_2:Rx is excited.

IV. ON-BODY PERFORMANCE ANALYSIS

A. BENDING ANALYSIS

The semi-flexible nature of the substrate material used for the proposed prototype provides sufficient flexibility to accommodate moderate bending, as validated by prior research [35], thereby enabling seamless integration into body-worn applications. Figure 11 shows the $|S_{11}|; |S_{22}|$ and $|S_{21}|$ results when the proposed antenna is rotated along $-45°$ and bent at three radii ($R = 40$, 50, and 60 mm). Here, the bending results are compared with the antenna's unbent (flat) state ($R = \infty$).

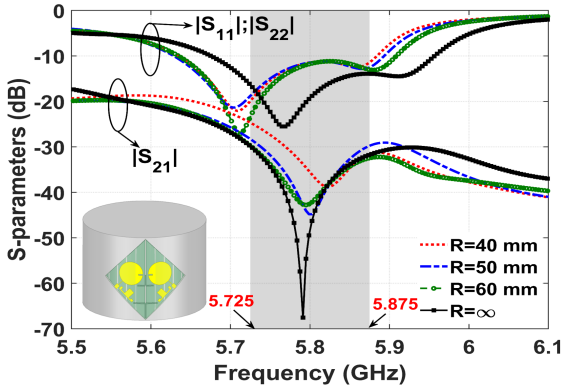

FIGURE 11. Simulated S-parameters for different bending radii.

The results demonstrate that although the resonant frequency downshifts and the CD ($|S_{21}|$) upshifts as the bending radius decreases, the antenna maintains its impedance bandwidth ($|S_{11}|; |S_{22}| < -10$ dB) and continues to operate effectively within the $5.725 - 5.875$ GHz ISM band for all bending radii. In addition, the isolation between P_1:Tx and P_2:Rx remains below -26 dB across the desired band, which demonstrates its suitability for full-duplex WBAN applications.

B. MEASURED S-PARAMETERS ON SUBJECT'S BODY

Here, the effect of the wearer's body on the proposed antenna is analyzed by placing it on various parts of the subject, as shown in Figure 12(a).

Figure 12(b) shows the measured $|S_{11}|; |S_{22}|$ and $|S_{21}|$ results when the proposed antenna is mounted on the arm, chest, and leg. Here, despite the influence of human tissue,

This article has been accepted for publication in IEEE Open Journal of Antennas and Propagation. This is the author's version which has not been fully edited and content may change prior to final publication. Citation information: DOI 10.1109/OJAP.2025.3648623

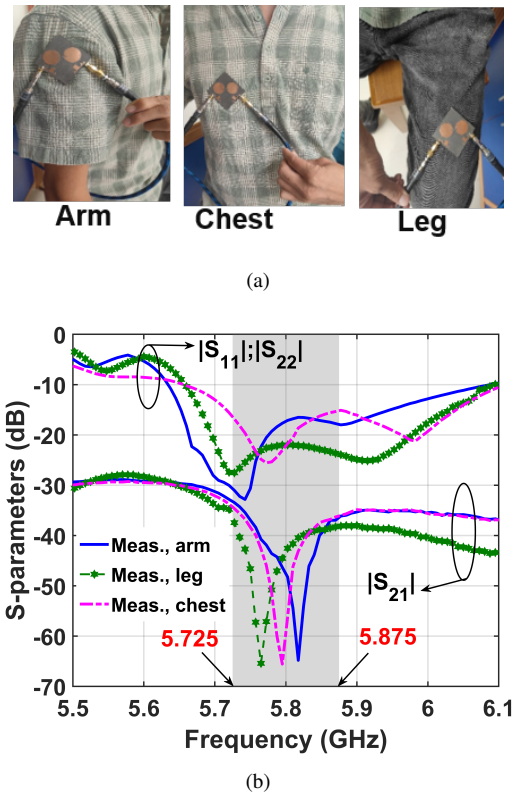

FIGURE 12. **Proposed antenna (a) Mounted on a human. (b) The effect on measured S-parameters.**

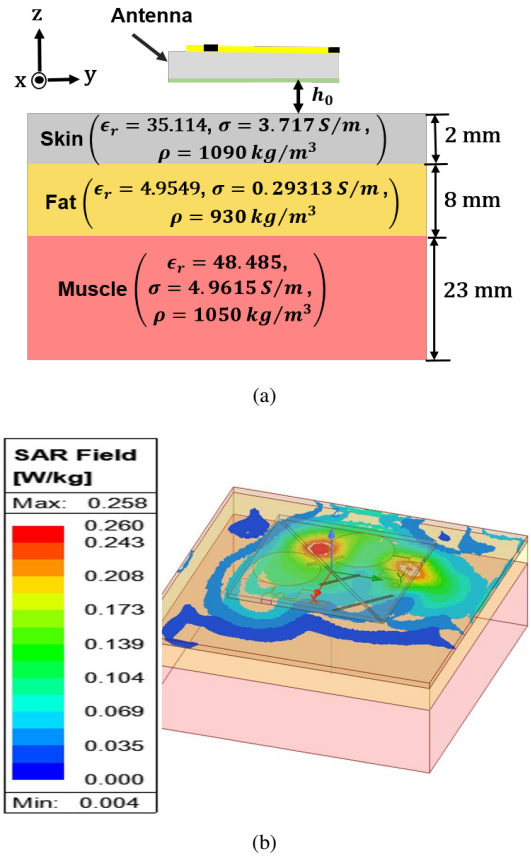

FIGURE 13. **(a) Horizontal cross-section of human phantom detailing the antenna over three layers of tissue. (b) Simulated 1 g averaged SAR with $h_0 = 4$ mm.**

the antenna effectively covers the entire 5.8 GHz ISM band while maintaining an isolation of $|S_{21}|$ below -33 dB. These results demonstrate that the proposed design effectively maintains stable bandwidth and high isolation between ports even when worn on lossy human tissues.

C. SAR ANALYSIS

The SAR (W/kg) is a key metric that quantifies the EM energy absorbed by human tissue and assesses potential health risks associated with EM exposure. The SAR can be computed using [4]

$$SAR = \frac{\sigma \left|\vec{E}\right|^2}{\rho} \tag{14}$$

where $\vec{E}$, σ, and ρ denote the electric field (V/m), conductivity (S/m), and mass density (kg/m^3) of the tissues, respectively. To ensure the wearer's safety, the proposed design is analyzed on a three-layer human tissue phantom (90 mm $\times$ 90 mm $\times$ 33 mm) replicating part of the user's body. Here, the antenna is mounted 4 mm above the phantom, and the tissue characteristics and thicknesses are detailed in Figure 13(a) [4].

Moreover, the SAR value must comply with the IEEE C95.1-2005 standard, which uses an input power of 100 mW [26]. The peak value of the simulated SAR for the proposed antenna is 0.258 W/kg, as shown in Figure 13(b), which is well below the prescribed safety limit. This ensures safe

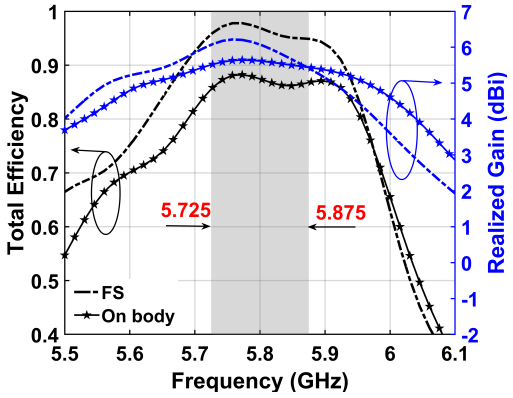

FIGURE 14. **Simulated efficiency and realized gain (dBi) of the proposed design.**

operation of the antenna. Furthermore, Figure 14 shows the simulated total efficiency and realized gain of the proposed design in free space (FS) and on-body environments. Note that a reduction in efficiency is observed when the antenna is mounted on the human body, which is attributed to the high dielectric properties and conductivity of human tissue at 5.8 GHz, as shown in Figure 13(a). The realized gain is minimally affected with a reduction of approximately 0.4 dBi at the center frequency of 5.8 GHz in the ISM

band. Nonetheless, the total efficiency remains greater than 84% within the desired frequency band, even under on-body conditions.

V. MIMO PERFORMANCE

In this section, the effectiveness and performance of the proposed design are evaluated by computing key MIMO performance metrics, including the envelope correlation coefficient (ECC), diversity gain (DG), total active reflection coefficient (TARC), and channel capacity loss (CCL). The ECC quantifies the level of correlation between the antenna radiation patterns and is critical in terms of ensuring diversity performance. A lower ECC value (typically less than 0.5) indicates better isolation and minimal correlation. Using the radiation pattern (Section III-C) method, the ECC can be calculated using [25], [31]

$$\mathrm{ECC}(j,k) = \frac{\left|\int\int_{4\pi}\left[\vec{F}_j(\theta,\phi)^* \vec{F}_k(\theta,\phi)\right]d\Omega\right|^2}{\left(\int\int_{4\pi}\left|\vec{F}_j(\theta,\phi)\right|^2 d\Omega\right)\cdot\left(\int\int_{4\pi}\left|\vec{F}_k(\theta,\phi)\right|^2 d\Omega\right)} \tag{15}$$

where $\vec{F}_j(\theta,\phi)$ and $\vec{F}_k(\theta,\phi)$ are the far-field radiation patterns of the j-th and k-th antenna, respectively, $d\Omega$ is the solid angle, and * corresponds to the Hermitian product operator. In contrast, the DG describes the improvement in signal reliability due to diversity and is determined using [25], [28]

$$DG = 10\sqrt{\left(1-\mathrm{ECC}^2\right)}. \tag{16}$$

Note that high DG value is desired for better MIMO performance. In addition, when all antenna elements in a multi-port antenna system are active simultaneously, they can affect each other's performance considerably. In such cases, relying solely on the S-parameter is insufficient to fully evaluate the antenna's effectiveness. To address this limitation, the TARC is employed as a more comprehensive parameter to assess antenna performance, which can be obtained using [28]

$$TARC = \sqrt{\frac{1}{2}\left[(S_{11}+S_{12})^2 + (S_{21}+S_{22})^2\right]}. \tag{17}$$

The proposed design is also evaluated in terms of the CCL. For a MIMO system, this refers to the maximum data rate that can be achieved reliably over a communication channel. The CCL can be computed as [11], [28]

$$C_{loss} = -\log_2\left(\det\left(\gamma^R\right)\right) \tag{18}$$

where $\gamma^R = \begin{pmatrix} R_{11} & R_{12} \\ R_{21} & R_{22} \end{pmatrix}$, $R_{jj} = 1 - \left(|S_{11}|^2 + |S_{22}|^2\right)$ and

$$R_{jk} = -\left(S_{jj}^* S_{jk} + S_{kj}^* S_{kk}\right)$$

for $j,k = 1$ or 2.

The plots in Figures 15(a) and 15(b) show the simulated results of the ECC, CCL, TARC, and DG. As can be seen, throughout the entire ISM band, the proposed MIMO antenna exhibits an extremely low ECC value (less than 0.0002) and a high DG value of up to 9.999 dB. Furthermore,

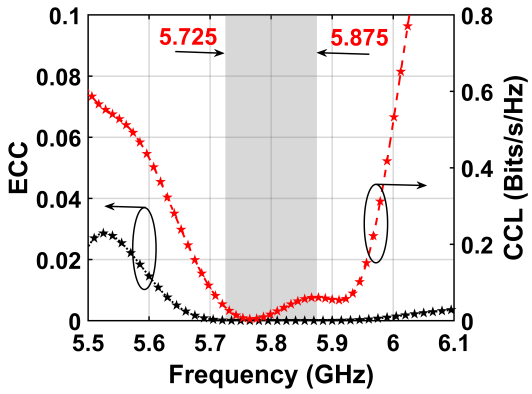

(a)

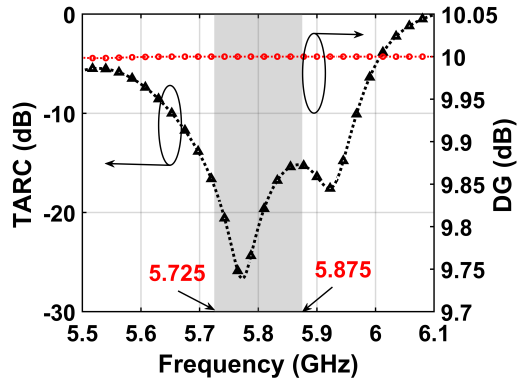

(b)

FIGURE 15. Simulated diversity performance for the proposed design (a) ECC and CCL. (b) TARC and DG.

the CCL remains below 0.16 b/s/Hz, which is below the acceptable CCL value of 0.4 b/s/Hz [28], and the TARC value remains below -10 dB across the band. These results quantitatively validate the robustness of the proposed design with respect to its MIMO capability.

A comparison study of existing wearable MIMO/wearable full-duplex MIMO designs with the proposed design is summarized in Table 1. As can be seen, the structure of the proposed polarization controlled dual-polarized MIMO antenna with enhanced isolation for full-duplex WBANs, is simpler than the compared designs [21], [31]. In addition, the proposed antenna achieves higher isolation than [14], [22], [23], [29], [30] while complying with SAR limit and exhibiting good bending tolerance when wrapped around the human body. The proposed design realizes isolation that is greater than 33 dB across the ISM band of $5.725-5.875$ GHz with a simpler structure than existing designs [22], [23] that rely on metallic vias. The proposed antenna achieves a peak isolation of approximately 67 dB with an edge-to-edge (E-E) spacing of $0.09\lambda_0$ while maintaining high efficiency and extremely low ECC, thereby ensuring superior performance in full-duplex MIMO systems. The realized gain of the proposed design is comparable to that of other reported antennas summarized in Table 1. These enhancements establish the

TABLE 1. Comparison study of various wearable MIMO/wearable full-duplex MIMO designs with the proposed antenna.

Ref.	Size (λ_0^3)	Isolation (dB)	Gain (dBi)	Dual Sense	E-E (λ_0)	SAR (W/kg)	Total Efficiency (%)	ECC	Circuit Model
[14]	$1.14 \times 0.57 \times 0.02$	26	4.7	No	0.1	NR	NR	< 0.01	No
[22]	$\pi \times 0.78^2 \times 0.02$	25	2.9/8.8	No	–	0.09*	54.7/78.5′	No	No
[23]	$0.6 \times 0.6 \times 0.02^{\dagger}$	28	4.2	Yes	0.06	$0.108^{\ddagger}$	> 40**	< 0.02	Yes
[29]	$3.3 \times 2.06 \times 0.05$	20	6.1	Yes	0.7	$2.18/1.64^{\diamond}$	$> 80'$	< 0.003	No
[30]	$0.31 \times 0.31 \times 0.02$	12	2.79	Yes	–	$0.22^{\ddagger}$	> 27	< 0.01	No
Prop.	$0.93 \times 0.93 \times 0.03$	33 (PI∼ 67)	6.01	Yes	0.09	0.258	> 84	< 0.0002	Yes

λ_0: corresponding to the center frequency; PI: Peak isolation; E-E: Edge-to-edge distance; NR: not reported; † guide wavelength at the dominant mode operating frequency ; ‡250 mW input power; * input power not mentioned; ** estimated from the graph; $\diamond$ 50 mW input power at 27.10 GHz and 29.53 GHz; 'radiation efficiency.

proposed antenna as a more efficient and practical solution for WBAN applications.

VI. CONCLUSION

This paper has proposed a polarization controlled dual-polarized MIMO antenna with enhanced isolation for a full-duplex WBAN operating in the 5.8 GHz ISM band. The proposed antenna design achieves good impedance matching and bandwidth by slotting twin circular patches and incorporating stepped elements adjacent to their feeding terminals. In addition, advanced polarization control of each antenna element comprising the MIMO is realized by embedding tailored T-shaped strips within transversal slots of a main diagonal cut in the ground plane. This effectively steers surface currents in a direction that is favorable for the desired polarization, and thereby improving inter-port isolation. The proposed antenna, measured experimentally in free space, demonstrates practical isolation improvement greater than 5 dB compared with existing designs, achieving inter-port isolation better than 33 dB for the 150 MHz bandwidth with a peak isolation of approximately 67 dB. The performance evaluation indicates low ECC, high DG, and acceptable TARC and CCL values. Furthermore, the proposed antenna was tested under structural deformation by bending it along the -45° direction, and a SAR value of 0.258 W/kg, obtained through analysis on a human phantom, confirms compliance with safety standards. These results validate the proposed antenna's robustness with good bending tolerance, making it a potential solution for wearable full-duplex WBAN applications. The optimized isolation and advanced polarization control enhance signal integrity and ensure reliable operation under wearable operating conditions. In next-generation wireless systems, where spatial constraints limit the feasibility of higher-order MIMO configurations, the proposed concept allows for good scalability towards multi-element antenna designs for higher MIMO data rates.

REFERENCES

[1] P. S. Hall, Y. Hao, Y. I. Nechayev, A. Alomainy, C. C. Constantinou, C. Parini, M. R. Kamarudin, T. Z. Salim, D. T. Hee, R. Dubrovka, A. S. Owadally, W. Song, A. Serra, P. Nepa, M. Gallo, and M. Bozzetti, "Antennas and propagation for on-body communication systems," *IEEE Antennas Propag. Mag.*, vol. 49, no. 3, pp. 41–58, 2007.

[2] D. H. Werner and Z. H. Jiang, *Electromagnetics of body area networks: antennas, propagation, and RF systems*. John Wiley & Sons, 2016.

[3] C.-X. Mao, S. Gao, and Y. Wang, "Dual-band full-duplex TX/RX antennas for vehicular communications," *IEEE Trans. Veh. Technol.*, vol. 67, no. 5, pp. 4059–4070, 2018.

[4] A. Thakur, A. Sharma, and I. J. G. Zuazola, "A wearable circulator-like circularly polarised antenna for full-duplex wireless body area network applications," *IET Microw. Antennas Propag.*, vol. 18, no. 11, pp. 838–848, 2024.

[5] C.-X. Mao, D. Vital, D. H. Werner, Y. Wu, and S. Bhardwaj, "Dual-polarized embroidered textile armband antenna array with omnidirectional radiation for on-/off-body wearable applications," *IEEE Trans. Antennas Propag.*, vol. 68, no. 4, pp. 2575–2584, 2020.

[6] A. Thakur and A. Sharma, "Low-profile orthogonal-ports dual-polarized antenna for full-duplex WBAN applications," in *2024 15th Int. Conf. on Computing, Communication and Networking Technologies (ICCCNT),* Kamand, India, 2024, pp. 1–4.

[7] H. Lee, J. Tak, and J. Choi, "Wearable antenna integrated into military berets for indoor/outdoor positioning system," *IEEE Antennas Wireless Propag. Lett.*, vol. 16, pp. 1919–1922, 2017.

[8] C. Mendes and C. Peixeiro, "A dual-mode single-band wearable microstrip antenna for body area networks," *IEEE Antennas Wireless Propag. Lett.*, vol. 16, pp. 3055–3058, 2017.

[9] D. Wen, Y. Hao, M. O. Munoz, H. Wang, and H. Zhou, "A compact and low-profile MIMO antenna using a miniature circular high-impedance surface for wearable applications," *IEEE Trans. Antennas Propag.*, vol. 66, no. 1, pp. 96–104, 2018.

[10] E. Rajo-Iglesias, O. Quevedo-Teruel, and L. Inclan-Sanchez, "Mutual coupling reduction in patch antenna arrays by using a planar EBG structure and a multilayer dielectric substrate," *IEEE Trans. Antennas Propag.*, vol. 56, no. 6, pp. 1648–1655, 2008.

[11] S. Arulmurugan, S. K. Tr, J. Sidén, and Z. C. Alex, "Circular polarized dual-band wearable screen-printed MIMO antenna integrated with AMC for WBAN communications," *IEEE Open J. Antennas Propag.*, 2024.

[12] M. Alibakhshikenari, M. Vittori, S. Colangeli, B. S. Virdee, A. Andújar, J. Anguera, and E. Limiti, "EM isolation enhancement based on metamaterial concept in antenna array system to support full-duplex application," in *2017 IEEE Asia Pacific Microwave Conference (APMC),* Kuala Lumpur, Malaysia, 2017, pp. 740–742.

[13] M. Alibakhshikenari, M. Khalily, B. S. Virdee, C. H. See, R. A. Abd-Alhameed, and E. Limiti, "Mutual-coupling isolation using embedded metamaterial EM bandgap decoupling slab for densely packed array antennas," *IEEE Access*, vol. 7, pp. 51827–51840, 2019.

[14] I. Adam, M. R. Kamarudin, A. H. Rambe, N. Haris, H. A. Rahim, W. Z. A. Wan Muhamad, A. M. Ismail, M. Jusoh, and M. N. M. Yasin, "Investigation on wearable antenna under different bending conditions for wireless body area network (WBAN) applications," *Int. J. Antennas Propag.*, vol. 2021, pp. 1–9, 2021.

[15] S. Zhang, S. N. Khan, and S. He, "Reducing mutual coupling for an extremely closely-packed tunable dual-element PIFA array through a resonant slot antenna formed in-between," *IEEE Trans. Antennas Propag.*, vol. 58, no. 8, pp. 2771–2776, 2010.

[16] Y. He and Y. Li, "Compact co-linearly polarized microstrip antenna with fence-strip resonator loading for in-band full-duplex systems," *IEEE Trans. Antennas Propag.*, vol. 69, no. 11, pp. 7125–7133, 2021.
[17] D. Wu, S. W. Cheung, Q. L. Li, and T. I. Yuk, "Decoupling using diamond-shaped patterned ground resonator for small MIMO antennas," *IET Microw. Antennas Propag.*, vol. 11, no. 2, pp. 177–183, 2017.
[18] M. G. N. Alsath, M. Kanagasabai, and B. Balasubramanian, "Implementation of slotted meander-line resonators for isolation enhancement in microstrip patch antenna arrays," *IEEE Antennas Wireless Propag. Lett.*, vol. 12, pp. 15–18, 2012.
[19] H. Nawaz and I. Tekin, "Dual-polarized, differential fed microstrip patch antennas with very high interport isolation for full-duplex communication," *IEEE Trans. Antennas Propag.*, vol. 65, no. 12, pp. 7355–7360, 2017.
[20] Y.-M. Zhang and J.-L. Li, "Differential-series-fed dual-polarized traveling-wave array for full-duplex applications," *IEEE Trans. Antennas Propag.*, vol. 68, no. 5, pp. 4097–4102, 2020.
[21] Y. Chen, C. Ding, Y. Jia, and Y. Liu, "Antenna/propagation domain self-interference cancellation (SIC) for in-band full-duplex wireless communication systems," *Sensors*, vol. 22, no. 5, pp. 1–18, 2022.
[22] G.-P. Gao, J.-M. Bai, L.-J. Jin, W.-D. Guo, G. Ma, and B. Hu, "A compact dual port circularly polarized MIMO antenna for on-/off-body WBAN applications," *IEEE Antennas Wireless Propag. Lett.*, pp. 1–5, 2025.
[23] D. Chaturvedi, P. Jadhav, A. A. Althuwayb, and K. Aliqab, "A compact 2-port QMSIW cavity-backed MIMO antenna with varied frequencies using CSRR-slot angles for WBAN application," *IEEE Access*, vol. 12, pp. 100506–100514, 2024.
[24] J. C. Dash and D. Sarkar, "A colinearly polarized full-duplex antenna with extremely high Tx–Rx isolation," *IEEE Antennas Wireless Propag. Lett.*, vol. 21, no. 12, pp. 2387–2391, 2022.
[25] A. K. Pandey, R. K. Gangwar, and R. K. Chaudhary, "A compact SD-QMSIW-based self-diplexing MIMO antenna using two modified l-shaped slots as radiators for IoT applications," *IEEE Internet Things J.*, vol. 12, no. 3, pp. 2385–2394, 2025.
[26] C. X. Mao, Y. Zhou, Y. Wu, H. Soewardiman, D. H. Werner, and J. S. Jur, "Low-profile strip-loaded textile antenna with enhanced bandwidth and isolation for full-duplex wearable applications," *IEEE Trans. Antennas Propag.*, vol. 68, no. 9, pp. 6527–6537, 2020.
[27] A. Kumar Biswas and U. Chakraborty, "Compact wearable MIMO antenna with improved port isolation for ultra-wideband applications," *IET Microw. Antennas Propag.*, vol. 13, no. 4, pp. 498–504, 2019.
[28] S. Kumar, D. Nandan, K. Srivastava, S. Kumar, H. Singh, M. Marey, H. Mostafa, and B. K. Kanaujia, "Wideband circularly polarized textile MIMO antenna for wearable applications," *IEEE Access*, vol. 9, pp. 108601–108613, 2021.
[29] R. N. Tiwari, V. Kaim, P. Singh, T. Khan, and B. K. Kanaujia, "Semi-flexible diversified circularly polarized millimeter-wave MIMO antenna for wearable biotechnologies," *IEEE Trans. Antennas Propag.*, 2023.
[30] H. Li, S. Sun, B. Wang, and F. Wu, "Design of compact single-layer textile MIMO antenna for wearable applications," *IEEE Trans. Antennas Propag.*, vol. 66, no. 6, pp. 3136–3141, 2018.
[31] U. Ullah, I. B. Mabrouk, and S. Koziel, "Enhanced-performance circularly polarized MIMO antenna with polarization/pattern diversity," *IEEE Access*, vol. 8, pp. 11887–11895, 2020.
[32] M. E. Munir, M. M. Nasralla, and M. A. Esmail, "Four port tri-circular ring MIMO antenna with wide-band characteristics for future 5G and mmwave applications," *Heliyon*, vol. 10, no. 8, 2024.
[33] J. C. Dash and D. Sarkar, "Microstrip patch antenna system with enhanced inter-port isolation for full-duplex/MIMO applications," *IEEE Access*, vol. 9, pp. 156222–156228, 2021.
[34] K. Turbic, L. M. Correia, and M. Beko, "A channel model for polarized off-body communications with dynamic users," *IEEE Trans. Antennas Propag.*, vol. 67, no. 11, pp. 7001–7013, 2019.
[35] M. A. B. Abbasi, S. S. Nikolaou, M. A. Antoniades, M. Nikolić Stevanović, and P. Vryonides, "Compact EBG-backed planar monopole for BAN wearable applications," *IEEE Trans. Antennas Propag.*, vol. 65, no. 2, pp. 453–463, 2017.